World Scientific
www.worldscientific.com

Improved Incompressible Material Point Method
Based on Particle Density Correction

Fan Zhang

Xi'an Modern Chemistry Research Institute
Xi'an 710065, P. R. China

Xiong Zhang*

School of Aerospace Engineering
Tsinghua University, Beijing 100084, P. R. China
xzhang@tsinghua.edu.cn

Kam Yim Sze

Department of Mechanical Engineering
The University of Hong Kong, Pokfulam, Hong Kong, P. R. China

Yong Liang and Yan Liu

School of Aerospace Engineering
Tsinghua University, Beijing 100084, P. R. China

In the incompressible material point method (iMPM), the momentum equations were solved at the background grid nodes while the divergence-free conditions were enforced at grid cell centers. The density of each particle was assumed to be constant but the particles could distribute nonuniformly in space over time. Therefore, the fluid density would be nonuniform and violate the incompressible condition. In this paper, the original iMPM is improved by explicitly imposing the density-invariant condition. A new particle shifting scheme is proposed for particle density correction. Particles are shifted along their density gradient to guarantee that the density field of the fluid is constant and the momentum is conserved. The proposed method has been implemented in our MPM code, and validated by simulating a dam breaking inside a tank, another dam breaking with an obstacle and a sloshing problem.

Keywords: Incompressible material point method; kernel function approximation; density-invariant condition; divergence-free condition.

---

*Corresponding author.

1. Introduction

Fluid flow with free surface has been a hot and challenging issue in computational fluid dynamics. Free surface flows are abundant in ship hydrodynamics, aerospace engineering, hydraulic engineering, mechanical engineering, petrochemical and civil engineering, etc. The meshfree/meshless methods such as the material point method (MPM) [Lian *et al.* (2011); Mast *et al.* (2012); Li *et al.* (2014); Chen *et al.* (2015); Zhang *et al.* (2017)], smoothed particle hydrodynamics (SPH) [Monaghan (1994); Morris *et al.* (1997); Shao and Lo (2003); Colin *et al.* (2006); Lee *et al.* (2008); Solenthaler and Pajarola (2009); Xu *et al.* (2009); Asai *et al.* (2012); Chen *et al.* (2013); Ihmsen *et al.* (2014); Liu and Li (2016)], moving particle semi-implicit (MPS) [Koshizuka and Oka (1996); Koshizuka *et al.* (1998); Pan *et al.* (2008); Tanaka and Masunaga (2010); Khayyer and Gotoh (2011)], and finite point method (FPM) [Onate *et al.* (1996)] have progressed significantly in simulating the nearly incompressible or fully incompressible fluid problems.

The MPM proposed by Sulsky *et al.* [1994] is an extension of fluid implicit particle (FLIP)/particle in cell (PIC) method [Harlow (1964); Brackbill and Ruppel (1986)] from fluid mechanics to solid mechanics. The MPM merges the advantages of both Eulerian and Lagrangian methods. It is promising in handling large deformation problems, such as impact/contact [Burghardt *et al.* (2010); Bardenhagen *et al.* (2001); Huang *et al.* (2011); Zhou *et al.* (2013)], penetration [Lian *et al.* (2011, 2014)], hypervelocity impact [Huang *et al.* (2008); Ma *et al.* (2009a); Liu *et al.* (2015, 2016)], cracks and fracture [Chen *et al.* (2002); Tan and Nairn (2002); Guo and Nairn (2004); Nairn (2007); Gilabert *et al.* (2011)], compressible gas dynamics [York *et al.* (2000); Hu and Chen (2006); Ma *et al.* (2009b); Tran *et al.* (2010)]. For the nearly incompressible fluid, Li *et al.* [2014] proposed a weak compressible MPM (WCMPM) which uses a weakly compressible equation of state (EOS) in MPM. By incorporating a grid-based contact algorithm into the WCMPM, they studied the sloshing phenomenon in a container with specified motion. Mast *et al.* [2012] have discussed how to mitigate the kinematic locking using the multi-field variational principle in nearly incompressible flow simulations. Chen *et al.* [2015] improved the coupling scheme of finite element method with MPM to simulate the contact between fluid and solid. Note worthily, WCMPM has encountered the following difficulties: (1) The weakly compressible EOS relates the pressure to the density of a fluid by an artificial sound speed, which is normally taken as 10 times higher than the maximum fluid velocity in order to reduce the density fluctuation down to 1% [Monaghan (1994)]. Thus, the critical time step size of the explicit time integration is very small and the computational cost is considerably high. (2) As a large artificial sound speed was used in WCMPM, a small density fluctuation would lead to a large pressure change followed by significant pressure oscillations. (3) The material surface is not explicitly tracked inside one cell, so it is difficult to accurately impose the pressure boundary conditions on the free surface.

To overcome the aforementioned shortcomings of the WCMPM, Zhang *et al.* [2017] proposed a fully incompressible material point method (iMPM) based on the operator splitting scheme. By assuming that the fluid density is constant, the pressure satisfying the divergence-free condition was obtained from the pressure Poisson equations (PPEs). It has been proved that the iMPM is much more accurate and efficient than the WCMPM in solving free surface flow problems [Zhang *et al.* (2017)]. However, in the iMPM, the fluid density is obtained as a summation of the delta functions centered at the particles. The initial uniformly distributed particles may become nonuniformly distributed over time. Therefore, the density-invariant condition in the fluid domain was not satisfied. In the iMPM, there is no internal force applied between particles to maintain the uniformity of particle distribution. Nonuniform distribution of particles could lead to numerical instability and artificial changes in fluid volume.

The above problem exists in most particle methods for incompressible fluid if the density-invariant condition is not imposed explicitly. In the SPH framework, the original SPH uses a stiff EOS to simulate the nearly incompressible fluid like that in WCMPM. However, a slight density variation will lead to a large pressure fluctuation and disorder of particles [Monaghan (1994); Morris *et al.* (1997); Lee *et al.* (2008); Yang *et al.* (2012)]. Solenthaler and Pajarola [2009] proposed a predictive–corrective incompressible SPH (PCISPH) method without invoking an EOS. The particle pressures were computed iteratively until the density converge to physical constant value. Thus, the density-invariant condition is satisfied. Many versions of incompressible SPH (ISPH) solve a PPE obtained from the divergence-free condition [Cummins and Rudman (1999); Colin *et al.* (2006); Chen *et al.* (2013)]. However, particle clustering could happen due to the spatial truncation error [Xu *et al.* (2009)]. Shao and Lo [2003] proposed a density-invariant ISPH method which uses the density difference as the source term in the PPE instead of the divergence of flow velocity field. Recently, Ihmsen *et al.* [2014] proposed a new implicit ISPH method which combines the symmetric SPH pressure force and continuity equation to obtain a discretized form of the PPE. The density invariance of particles can be greatly improved. A better scheme in which a hybrid PPE source including both the velocity divergence term and relative density variance term is proposed by Asai *et al.* [2012]. Numerical results show that the scheme can significantly improve the distribution of particles and velocity field accuracy [Gui *et al.* (2013, 2015)]. This hybrid idea has also been applied in the MPS method [Tanaka and Masunaga (2010); Khayyer and Gotoh (2011)]. Recently, Nair and Gaurav [2015] proposed a deformation gradient-based approach to preserve the particle volume and maintain density uniformity that was introduced in the ISPH method with divergence-free condition.

In the finite volume particle method (FVPM), Nestor *et al.* [2008] proposed a particle velocity correction which maintains the uniformity of the moving particle cloud by incorporating some extra diffusion terms to the total momentum. Xu *et al.* [2009] modified the Nestor's scheme by adding a small shift to the particle position

as that used in the SPH method. It can maintain accuracy and stability in high Reynolds number problems. In the PIC/FLIP method, Ando and Tsuruno [2011] and Ando *et al.* [2012] proposed a particle shift scheme by adding an anisotropic displacement to particle position to move particles along the direction of an SPH-like pressure force which is equivalent to a kind of spring force unrelated to the particle density. Recently, Um *et al.* [2014] proposed a sub-grid-based particle correction method to address the high-frequency errors in FLIP which ensures the proper distribution of the particles.

In this paper, the original iMPM is improved by explicitly imposing the density-invariant condition. The divergence-free condition is first enforced when solving the momentum equations at the background grid nodes. The density-invariant condition is then imposed at the end of each time step. The improved iMPM satisfies both the divergence-free condition and the density-invariant condition. Compared to the original divergence-free version of iMPM, the improved iMPM is more accurate and stable due to the explicit satisfaction of the density-invariant condition.

The remaining part of this paper is organized as follows. The governing equations for the iMPM are given in Sec. 2 and the Lagrangian particle density correction scheme is presented in details in Sec. 3. The numerical implementation of the proposed method is summarized in Sec. 4 whilst numerical examples are presented in Sec. 5 to validate the proposed method. Finally, conclusions are given in Sec. 6.

2. Incompressible Material Point Method

The traditional MPM is a hybrid method which makes use of both the Eulerian and Lagrangian descriptions. A material domain is discretized by a collection of Lagrangian particles moving through a Eulerian background grid, as shown in Fig. 1. The particles carry all state variables such as the position, velocity, strain and stress, whereas the grid serves as a computational scratch pad upon which gradients and spatial integrals are computed. At the beginning of each time step, the background grid is rigidly attached to the particles. The grid then deforms with the particles so that it can be viewed as a finite element discretization of the material domain. The momentum equations are solved on the grid, whose solution is used to update the kinematics variables of the particles. At the end of each time step, the deformed background grid is reset to its initial state for the next time step. Based on the
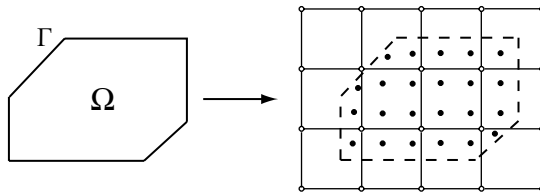
Fig. 1. MPM discretization of computational domain.

framework of the MPM, an iMPM was proposed by Zhang *et al.* [2017] in which operator splitting scheme was used to uncouple the pressure and velocity fields. The divergence-free condition was enforced in each fluid cell to establish the PPEs. The only difference between MPM and iMPM is the calculation of the fluid pressure. More details of the interpolations between the particles and the grid in explicit time step can be found in the published papers, Zhang *et al.* [2016, 2017].

2.1. *Governing equation*

Decomposing the stress $\boldsymbol{\sigma}$ into the sum of deviatoric stress $\boldsymbol{s}$ and hydrostatic pressure p, i.e., $\boldsymbol{\sigma} = -p\boldsymbol{I} + \boldsymbol{s}$, the momentum equation of a fluid can be written as

$$\rho\dot{\boldsymbol{v}} = -\nabla p + \nabla \cdot \boldsymbol{s} + \rho\boldsymbol{b}, \tag{1}$$

where $\boldsymbol{v}$ is the velocity, ρ is the density and $\boldsymbol{b}$ is the body force per unit mass. For fully incompressible fluid, the velocity field must satisfy the divergence-free condition, i.e.,

$$\nabla \cdot \boldsymbol{v} = 0. \tag{2}$$

2.2. *Operator splitting*

Using the operator splitting method, the computations of velocity and pressure fields can be decoupled. This method consists of two stages [Chorin (1968)]. In the first stage, the pressure gradient term is ignored in Eq. (1) to obtain an intermediate velocity field $\boldsymbol{v}^*$, namely

$$\rho\dot{\boldsymbol{v}}^* = (\nabla \cdot \boldsymbol{s} + \rho\boldsymbol{b}), \quad \boldsymbol{v}^*|_{\Gamma_v} = \bar{\boldsymbol{v}}, \tag{3}$$

where $\boldsymbol{v}$ is the velocity at time t^n and $\bar{\boldsymbol{v}}$ is the rigid wall velocity at background grid. For Newtonian fluid, the deviatoric stress is updated by

$$\boldsymbol{s} = 2u\dot{\boldsymbol{\varepsilon}}', \tag{4}$$

where coefficient of dynamic viscosity μ is constant and $\dot{\boldsymbol{\varepsilon}}'$ is the tensor of deviatoric strain rate.

In the second stage, the intermediate velocity $\boldsymbol{v}^*$ is corrected with the pressure gradient term to obtain the final solution v^{n+1}, namely

$$\boldsymbol{v}^{n+1} = \boldsymbol{v}^* - \frac{\triangle t}{\rho}\nabla p^{n+1}, \quad \boldsymbol{v}^{n+1}|_{\Gamma_v} = \bar{\boldsymbol{v}}, \tag{5}$$

which satisfies the divergence-free condition (2).

Equation (3) is independent of volumetric deformation, so that it can be solved using an explicit time integration scheme efficiently with a large time step. Thus, the intermediate grid nodal velocity $\boldsymbol{v}_I^*$ can be obtained as

$$\boldsymbol{v}_I^* = \boldsymbol{v}_I^n + \frac{\triangle t}{m_I}(\boldsymbol{f}_I^{\text{ext}} + \boldsymbol{f}_I^{\text{int,s}}), \tag{6}$$

where the subscript I denotes the background grid node, $\boldsymbol{v}^n$ is the velocity at time t^n,

$$\boldsymbol{f}_I^{\text{ext}} = \sum_{p=1}^{n_p} m_p N_{Ip} \boldsymbol{b}_p \tag{7}$$

is the external grid nodal force due to the body force such as gravity and $N_{Ip} = N_I(\boldsymbol{x}_p)$ is the grid shape function of node I evaluated at the location of particle p. Taking the eight-node brick element as an example, the grid shape functions are given by

$$N_I = \frac{1}{8}(1 + \xi\xi_I)(1 + \eta\eta_I)(1 + \zeta\zeta_I), \quad I = 1, 2 \ldots, 8, \tag{8}$$

where (ξ_I, η_I, ζ_I) are the natural coordinates of grid node I in the reference coordinate system ($\xi \in [-1, 1], \eta \in [-1, 1], \zeta \in [-1, 1]$),

$$\boldsymbol{f}_I^{\text{int,s}} = -\sum_{p=1}^{n_p} (\nabla N_{Ip})^{\text{T}} \boldsymbol{s}_p \frac{m_p}{\rho_p} \tag{9}$$

is the internal grid nodal force contributed by the deviatoric stress only like the viscous force.

2.3. *Pressure Poisson equations*

Substituting Eq. (5) into Eq. (2) results in the following PPE:

$$\nabla \cdot \boldsymbol{v}^* = \frac{\triangle t}{\rho} \nabla^2 p^{n+1}. \tag{10}$$

Equation (10) can be solved approximately by collocation at the cell centers. Thus, the terms $\nabla \cdot \boldsymbol{v}^*$ and $\nabla^2 p$ need to be evaluated at cell centers. Because the velocity is carried by the cell vertexes in MPM, the divergence of the intermediate velocity field $\boldsymbol{v}^*$ at cell center (i, j, k) can be approximated by the finite element approximation as

$$\nabla \cdot \boldsymbol{v}^*(\boldsymbol{x}_{i,j,k}) = \sum_I \boldsymbol{v}_I^* \cdot \nabla N_I(\boldsymbol{x}_{i,j,k}). \tag{11}$$

The second-order derivative of the pressure p with respect to x can be approximated at the cell center (i, j, k) by using the central difference method, i.e.,

$$\left(\frac{\mathrm{d}^2 p}{\mathrm{d}x^2}\right)_{i,j,k} = \frac{p_{i+1,j,k} + p_{i-1,j,k} - 2p_{i,j,k}}{\Delta x^2}, \tag{12}$$

where Δx is the cell side length in x direction. In this paper, cubic cells are used so that $\Delta x = \Delta y = \Delta z = dl$. Thus, the Laplacian $\nabla^2 p$ can be approximated at the

cell center (i, j, k) by using the seven-point stencil finite difference formula as

$$(\nabla^2 p)_{i,j,k} = \frac{p_{i+1,j,k} + p_{i-1,j,k} + p_{i,j+1,k} + p_{i,j-1,k} + p_{i,j,k+1} + p_{i,j,k-1} - 6p_{i,j,k}}{dl^2}.$$

(13)

Substituting Eqs. (11) and (13) into Eq. (10) leads to a system of linear equations which can be expressed as

$$\boldsymbol{A}\boldsymbol{p} = \boldsymbol{b},$$

(14)

where $\boldsymbol{A}$ is the coefficient matrix, $\boldsymbol{p}$ is a vector consisting of pressure at all cell centers, $\boldsymbol{b}$ is a vector consisting of the negative divergences of the intermediate velocity at each cell center. The matrix is symmetric and positive semi-definite. The equation can be solved efficiently by a preconditioned conjugate gradient (PCG) solver.

3. Particle Density Correction

In incompressible flows, the fluid density is spaciously uniform and constant over time. That is to say, the spacious density of the particles must remain invariant over time. However, in iMPM, only the divergence-free condition is imposed and the density invariance cannot be guaranteed. In the SPH, the internal forces between particles depend on the particle distribution and provide the mechanism to maintain the uniformity of the particles. Unfortunately, the momentum equations in iMPM are solved at the background grid nodes, i.e., the particles serve as quadrature points. Thus, there are no explicit internal forces between the particles to restore the uniformity of the particle distribution.

3.1. *Other particle shifting schemes*

Several particle shifting schemes, such as Xu's scheme and Ando's scheme, have been developed for other methods. They can be integrated into iMPM and be compared with our new scheme.

3.1.1. *Xu's scheme*

The idea of shifting the particles was first proposed in a meshfree method called FVPM by Nestor *et al.* [2008]. Xu *et al.* modified Nestor's scheme for the ISPH method [Xu *et al.* (2009)]. The particle convection distance and the particle distribution were taken into consideration so that the position shift vector reads

$$\Delta\boldsymbol{x}_p = C\alpha\boldsymbol{R}_p,$$

(15)

where C is a constant taken between 0.01 and 0.2, $\alpha = U_{\max}\Delta t$ is the maximum particle convection distance and $U_{\max}$ is the maximum particle velocity. The vector

$\boldsymbol{R}_p$ is determined by

$$\boldsymbol{R}_p = \sum_{j=1}^{N} \frac{\bar{r}_p^2}{r_{pj}^2} \boldsymbol{n}_{pj}, \tag{16}$$

where r_{pj} is the distance between particles p and j, $\bar{r}_p = \frac{1}{N} \sum_{j=1}^{N} r_{pj}$ is the average particle spacing in the neighborhood of p, $\boldsymbol{n}_{pj}$ is the unit distance vector between p and its neighbors j. The weighting function $\bar{r}_p^2 / r_{pj}^2$ was used to reduce the influence of remote neighboring particles.

3.1.2. *Ando's scheme*

Ando proposed a scheme in which the particle is shifted slightly along the direction of an SPH-like pressure force [Ando and Tsuruno (2011); Ando *et al.* (2012)]. The shift vector $\boldsymbol{\Delta x}_p$ was determined by

$$\Delta \boldsymbol{x}_p = \triangle t \gamma_s d_p \boldsymbol{R}_p, \tag{17}$$

where $\gamma_s = 50$ is the chosen stiffness of the displacement [Ando *et al.* (2012)], d_p is the smoothing length of particle p,

$$\boldsymbol{R}_p = \sum_{j=1}^{N} \frac{\boldsymbol{x}_p - \boldsymbol{x}_j}{|\boldsymbol{x}_p - \boldsymbol{x}_j|} W(\boldsymbol{x}_p - \boldsymbol{x}_j, d_p), \tag{18}$$

where $\boldsymbol{x}_p$ is the position of the particle that needs to be shifted, and $\boldsymbol{x}_j$ is the position of neighboring particles in the support domain of p.

Both Xu's and Ando's schemes are implemented in our MPM3D code to compare their performance with our improved scheme.

3.2. *Particle shifting*

To maintain the uniformity of the particle distribution, we redistribute the particles at the end of each time step to make the new density field equals the rest density ρ_0. The particle p will be shifted by $\Delta \boldsymbol{x}_p$. Accordingly, its density will change from $\rho(\boldsymbol{x}_p)$ to $\rho_0(\boldsymbol{x}_p + \Delta \boldsymbol{x}_p)$. Expanding the density $\rho_0(\mathbf{x}_p + \boldsymbol{\Delta x}_p)$ using Taylor series gives

$$\rho_0(\boldsymbol{x}_p + \Delta \boldsymbol{x}_p) = \rho(\boldsymbol{x}_p) + \Delta \boldsymbol{x}_p \cdot \nabla \rho_p + O(|\Delta \boldsymbol{x}_p|^2), \tag{19}$$

where $\nabla \rho_p \equiv \nabla \rho(\boldsymbol{x}_p)$. The shift vector $\Delta \boldsymbol{x}_p$ can be obtained from Eq. (19) as

$$\Delta \boldsymbol{x}_p = \beta c \boldsymbol{n}_{\nabla \rho_p}, \tag{20}$$

where the coefficient β is taken as 0.01 in this paper,

$$c = \frac{\rho_0 - \rho(\boldsymbol{x}_p)}{|\nabla \rho_p|} \tag{21}$$

and

$$\boldsymbol{n}_{\nabla \rho_p} = \frac{\nabla \rho_p}{|\nabla \rho_p|} \tag{22}$$

is the unit vector along the density gradient. Therefore, the shifted position of particle p is given as

$$\boldsymbol{x}_p^{\text{new}} = \boldsymbol{x}_p + \triangle \boldsymbol{x}_p. \tag{23}$$

To keep the velocity field consistent over the whole domain, the particle's velocity at its new position is recalculated from the grid nodal momentum as

$$\boldsymbol{v}_p^{\text{new}} = \chi \sum_{I=1}^{N} \boldsymbol{v}_I^{n+1} N_{pI}(\boldsymbol{x}_p^{\text{new}}) + (1.0 - \chi)(\boldsymbol{v}_p^n + \Delta \boldsymbol{v}_p(\boldsymbol{x}_p^{\text{new}})), \tag{24}$$

where the coefficient χ is taken as 0.03 in this paper [Ando *et al.* (2012); Zhu and Bridson (2005)].

3.3. *Density kernel approximation*

In Eq. (20), the density gradient is used to calculate the shift vector $\triangle \boldsymbol{x}_p$. In the standard MPM/iMPM, the density of a fluid at a point $\boldsymbol{x}$ is approximated as

$$\rho(\boldsymbol{x}) = \sum_{p=1}^{n_p} m_p \delta(\boldsymbol{x} - \boldsymbol{x}_p), \tag{25}$$

where n_p is the total number of particles; m_p and $\boldsymbol{x}_p$ are the mass and coordinate of particle p, respectively; and δ is the Dirac delta function. According to Eq. (25), the density field of the fluid domain is discontinuous due to the infinitesimal support domain of each particle. To calculate the density gradient, a continuous density field is constructed by employing the following kernel approximation:

$$\rho(\boldsymbol{x}) = \sum_{p=1}^{n_p} m_p W(\boldsymbol{x} - \boldsymbol{x}_p, h), \tag{26}$$

where W is the kernel function and h is the smooth length. Thus, the density gradient is

$$\nabla \rho(\boldsymbol{x}) = \sum_{p=1}^{n_p} m_p \nabla W(\boldsymbol{x} - \boldsymbol{x}_p, h). \tag{27}$$

In the traditional SPH method, bell-shaped spline kernels such as the following cubic spline kernel function have been commonly used [Monaghan (1985)]:

$$W_B(R, h) = a_d \begin{cases} \dfrac{2}{3} - R^2 + \dfrac{1}{2}R^3, & 0 \leq R < 1, \\[2mm] \dfrac{1}{6}(2 - R)^3, & 1 \leq R < 2, \\[2mm] 0, & R \geq 2. \end{cases} \tag{28}$$
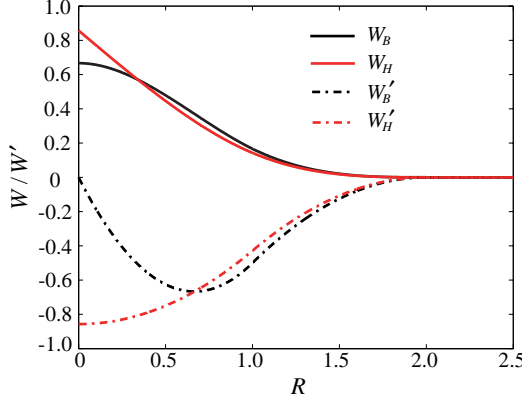
Fig. 2. Comparison of the kernel functions and their first derivatives.

In the expressions, $R = |\boldsymbol{x} - \boldsymbol{x}_p|/h$, $a_d = 1/h$, $15/7\pi h^2$ and $3/2\pi h^3$ for one-, two- and three-dimensional spaces, respectively. However, the first derivative of the cubic spline kernel is not monotonic as shown by the black dash-dot line in Fig. 2.

Physically, the particle closer to a point $\boldsymbol{x}$ should have larger weight $|\nabla W|$ for the density gradient of the point using Eq. (27). However, $|\nabla W_B|$ increases with R when $R < 2/3$, and then decreases. If the cubic spline kernel function W_B is used, the particle closer to the point $\boldsymbol{x}$ will have smaller weight $|\nabla W_B|$ when $R < 2/3$. Consequently, the shift vector (20) calculated using W_B as the kernel function may not be along the expected density gradient and may even be opposite to the expected density gradient. In other words, W_B may lead to unphysical particle clustering or voids, as shown in Fig. 3(a).

Liu *et al.* [Yang and Liu (2012); Yang *et al.* (2014)] employed the following hyperbolic-shaped kernel in their study

$$W_H(R, h) = a_d \begin{cases} R^3 - 6R + 6, & 0 \le R < 1, \\ (2 - R)^3, & 1 \le R < 2, \\ 0, & R \ge 2, \end{cases} \tag{29}$$

where $a_d = 1/7h$, $1/3\pi h^2$ and $15/62\pi h^3$ for one-, two- and three-dimensional spaces, respectively. The first derivative of W_H increases monotonically with R as shown by the red dash-dot line in Fig. 2. Employing W_H as the kernel function in calculating the density effectively eliminates the unphysical particle clustering or voids, as shown in Fig. 3(b).

3.4. *Boundary particle density correction*

There are two types of boundaries in the incompressible fluid flow with free surface, namely, the free surface and the rigid wall. The density of the fluid near the boundaries will be underestimated if Eq. (26) is used to construct the continuous density
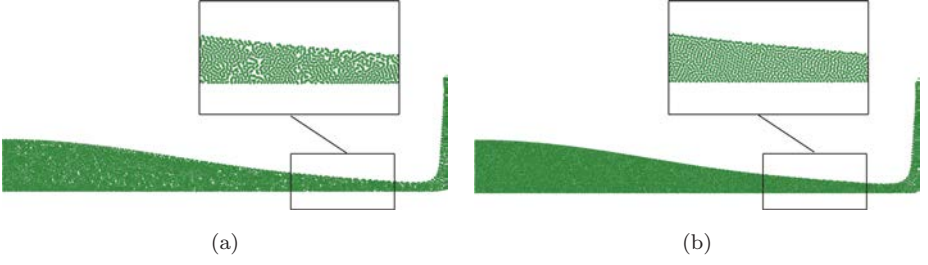
Fig. 3. Shifted particles using (a) the cubic spline kernel and (b) the hyperbolic-shaped kernel in dam breaking simulation.

field. Therefore, the obtained density gradient near the boundaries will point outward to the boundaries, and the particles near boundaries will be shifted outside the fluid region by using Eq. (20).

For particles near the free surface, the unit outward normal of the free surface should be subtracted from the estimated density gradient to guarantee shifting them within the fluid domain. In other words, the particles near the free surface will be shifted by

$$\Delta \boldsymbol{x}_p = \beta c [\boldsymbol{n}_{\nabla \rho_p} - (\boldsymbol{n}_{\nabla \rho_p} \cdot \boldsymbol{n}_{\nabla \varphi_p}) \boldsymbol{n}_{\nabla \varphi_p}], \tag{30}$$

where $\boldsymbol{n}_{\nabla \varphi_p} = \nabla \varphi_p / |\nabla \varphi_p|$ is the unit outward normal of the free surface calculated from the gradient of the level set function φ [Zhang *et al.* (2017)].

For particles near the rigid wall, the ghost particle scheme proposed by Akinci *et al.* [2012] is employed to correct the fluid density. A single layer of uniformly distributed ghost particles is created outside the rigid wall. The volume of a ghost particle g can be calculated by

$$V_g = \frac{m_g}{\sum_k m_k W_{gk}}, \tag{31}$$

where m_g is the mass of the ghost particle g, k denotes all the neighboring particle of g inside its kernel support domain. To attain a continuous density ρ_0 which is the rest density of the fluid, the mass of ghost particle g should take the value of

$$M_g(\rho_0) = \rho_0 V_g. \tag{32}$$

Therefore, the modified density of a fluid particle p near the rigid wall is

$$\rho_p = \sum_j m_p W_{pj} + \sum_k M_k(\rho_0) W_{pk}, \tag{33}$$

where j and k denote the neighboring fluid particles and neighboring ghost particles of the particle p, respectively.

4. Numerical Implementation

The explicit time integration for momentum equations can be used directly in the proposed scheme. The sound speed of viscosity, the body force, the velocity of

fluid flow as well as the Courant–Friedrichs–Lewy (CFL) condition are taken into account, the size of time step can be represented by

$$\Delta t = \alpha \min \left(\frac{d_c}{\|\boldsymbol{u}_p\|_{\max}}, \frac{d_c^2}{2\nu}, \sqrt{\frac{2d_c}{\|\boldsymbol{b}\|}} \right), \tag{34}$$

where $\|\boldsymbol{u}_p\|_{\max}$ is the maximum velocity of all fluid particles, the parameter $\nu = \frac{\mu}{\rho}$ is the kinematic viscosity of the fluid, d_c is the characteristic length which is set to be the size of cell dl, α is the dimensionless coefficient of CFL which is set to be 0.15 in this work. It should be noted that the term of the viscosity in Eq. (34) is very low for water, then $\|\boldsymbol{u}_p\|_{\max}$ and $\|\boldsymbol{b}\|$ are dominant to determine the size of the time step in the improved iMPM which is much larger than that in explicit MPM.

The implementation of the improved iMPM is summarized as follows:

(1) Initialize the background grid by resetting all the grid nodal variables to zero.
(2) Loop over all particles in the fluid domain to calculate their contributions to the masses and the momenta of the grid nodes by

$$m_I^n = \sum_p^{n_p} m_p N_{Ip}^n, \tag{35}$$

$$p_{iI}^n = \sum_p^{n_p} m_p v_{ip}^n N_{Ip}^n. \tag{36}$$

(3) Solve the grid nodal velocity at time t^n by

$$v_{iI}^n = p_{iI}^n / m_I^n. \tag{37}$$

(4) Calculate the intermediate grid nodal velocities v_i^* and impose the velocity boundary conditions using Eq. (3).
(5) Initialize the signed distance function and identify the fluid cell, air cell and free surface either based on the isocontour of particle spherical function or based on a user defined initial grid level set function, readers can see related articles from Foster and Fedkiw [2001], Zhang *et al.* [2017] for further details.
(6) Calculate the fluid cell divergence and solve the PPE (14) using a PCG solver.
(7) Update the corrected velocities v_{iI}^{n+1} using Eq. (5), and the calculation of pressure gradient can refer to Zhang *et al.* [2017].
(8) Update the particle velocities using a linear combination scheme [Zhu and Bridson (2005)], i.e.,

$$v_{ip}^{n+1} = \chi \sum_{I=1}^{n_g} v_{iI}^{n+1} N_{pI} + (1.0 - \chi)(v_{ip}^n + \Delta v_{ip}), \tag{38}$$

where $0 \leq \chi \leq 1$ is a coefficient taken to be 0.03 in this paper.
(9) Update the particle positions using RK3-TVD method [Shu and Osher (1988)] with the updated grid velocities v_i^{n+1}.

(10) Calculate the density of each particle using Eq. (26) with the hyperbolic-shaped kernel at time t^{n+1}.

(11) Estimate the gradient of particle density, and calculate the position shifting vector $\Delta \boldsymbol{x}_p$ using Eq. (20), Eq. (15) or Eq. (17).

(12) Recalculate the new position and velocity of all particles using Eqs. (23) and (24), respectively.

(13) Return to step 1 to start a new time step.

In the above implementation, the divergence-free condition is imposed in solving the PPE from step 4 to step 10, and the density-invariant condition is imposed by our proposed scheme explicitly from step 11 to step 13. The improved iMPM can satisfy the divergence-free condition and density-invariant condition simultaneously.

5. Numerical Examples

The improved iMPM has been implemented in our MPM3D code. Its improvements and advantages over the original iMPM are illustrated by several numerical examples in this section.

5.1. *Two-dimensional* (2D) *Dam breaking inside a tank*

The dam break experiment conducted by Zhou *et al.* [1999] and Lobovsk *et al.* [2014] is first simulated to evaluate the improved iMPM. A schematic diagram of the test is shown in Fig. 4. Before the experiment, water with depth 0.6 m was at rest in the 1.2 m long reservoir area on the left side of a flap. The reservoir and the flap are contained at left end of a rigid tank of length $l_0 = 3.22$ m and height 2.5 m. A background grid with 161×125 cells of side length 0.02 m is employed. The water density ρ, water viscosity μ and gravity g are 1.0×10^3 kg/m³, 1.01×10^{-3} Pa · s and 9.8 m/s², respectively. At time equal to zero, the flap is removed instantaneously and the column of water in the reservoir area crashes under the force of gravity.
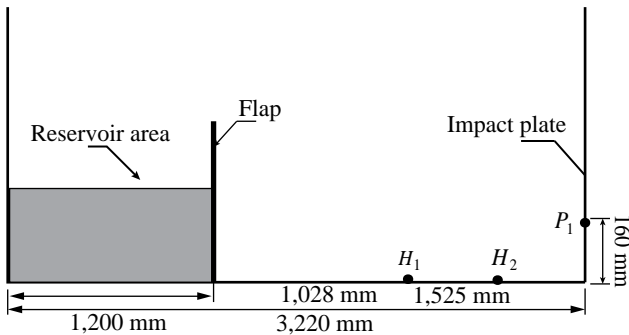
Fig. 4. Schematic diagram for 2D dam breaking.

In our simulations, 2×2 particles are initially placed inside each fluid cell. Thus, the water column is discretized by a total of 7,200 fluid particles. Moreover, 1,144 ghost particles are placed outside the fluid domain to correct the density of the particles near the rigid walls. Figure 5 compares the fluid profiles obtained by the original iMPM and the improved iMPM at different time steps. The flow profiles predicted by both methods can reflect the whole process including dam breaking, plunging wave and water merging. However, the particle distribution obtained by the improved iMPM is much more uniform than that of the original iMPM. The uneven particle distribution not only reduces the accuracy of velocity field but also leads to pressure oscillations. Furthermore, particle clustering and disordering lead to significant unphysical loss of fluid volume in the original iMPM. These problems
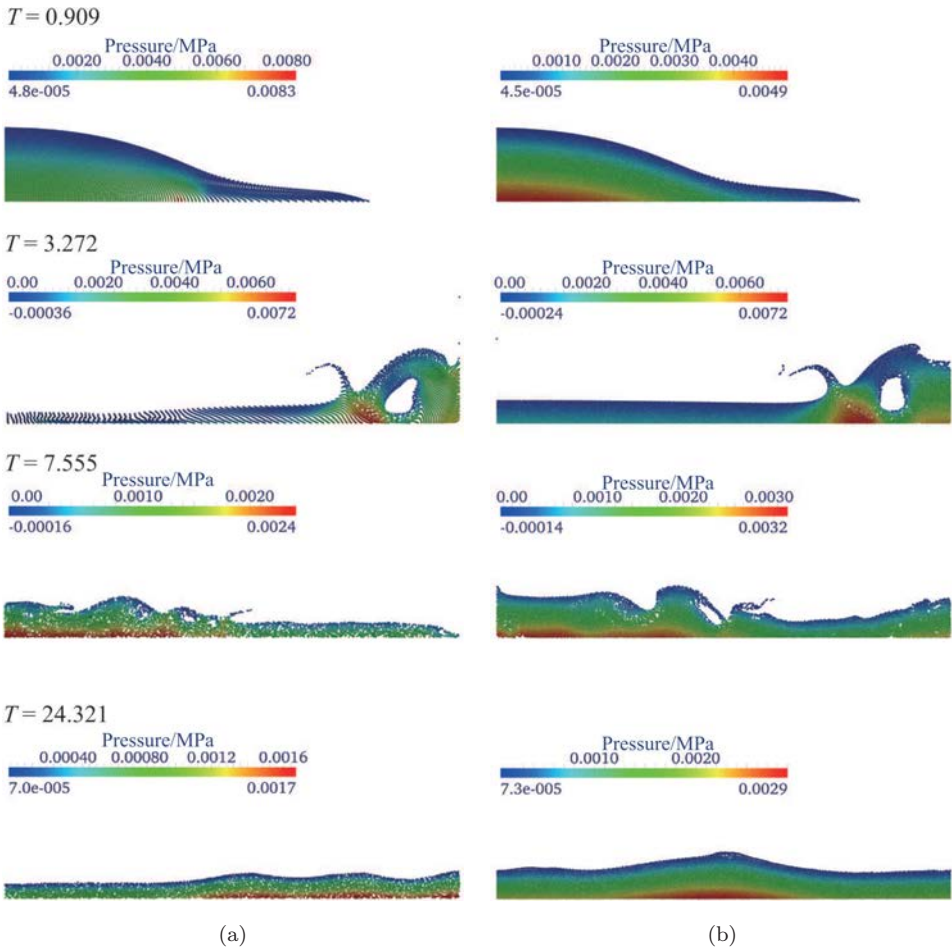
Fig. 5. Fluid profiles at different time instants obtained by (a) the original iMPM and (b) our improved iMPM.

can be mitigated by using more particles in each cell, like 4×4 particles in each cell, at the expense of significant higher computational cost. Our new scheme can maintain the numerical stability and accuracy by using as less particles as possible.

To compare the numerical results quantitatively, the following normalized density error and average velocity divergence error are defined:

$$E_{\text{den}}(t) = \frac{1}{N} \sum_{p=1}^{N} \left| \frac{\rho_0 - \rho(\boldsymbol{x}_p)}{\rho_0} \right|, \tag{39}$$

$$E_{\text{div}}(t) = \frac{1}{M} \sum_{i=1}^{M} |(\nabla \cdot \boldsymbol{v})_i|, \tag{40}$$

where N and M represent the number of fluid particles and the number of fluid cells, respectively. Note worthily, the density and velocity divergence errors are evaluated at the fluid particle and the fluid cell center, respectively.

Figure 6 compares the normalized particle density error obtained by the original iMPM with those of the improved iMPMs using different particle shifting schemes. The original iMPM leads to significant error in the particle density, which reaches up to 160%. On the contrary, the iMPM improved with the three particle shifting schemes reduce the particle density error significantly, which ranges from 6% to 32%. In terms of the minimum variation of density error over time, our shifting scheme is the optimized one among the three schemes as our scheme shifts the particle along the density gradient whilst those of Xu and Ando shift along a weighted direction.

Figure 7 further compares the fluid velocity errors. The peaks in the velocity divergence error curves are associated with the violent flow merger. Obviously, the particle shifting schemes can effectively decrease the velocity error and improve the accuracy of velocity field. Since the original iMPM has imposed the divergence-free condition, the improvement of new schemes in velocity field is not as remarkable as in the density invariance.
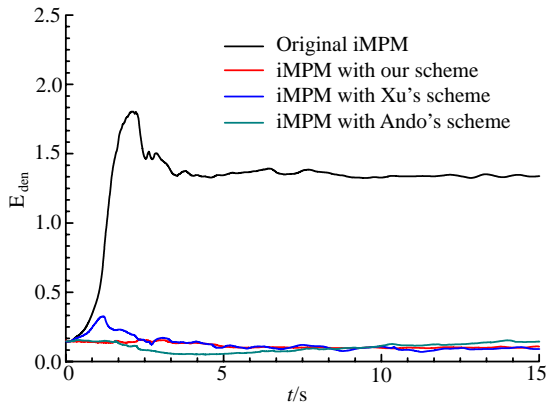
Fig. 6. Normalized particle density error.
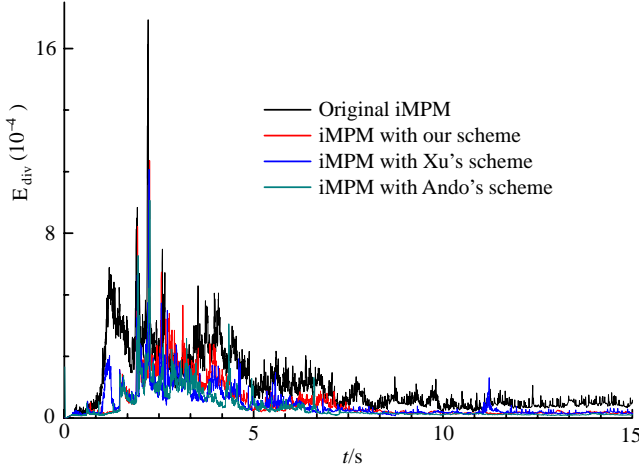
Fig. 7. Fluid cell average velocity divergence error.

Finally, the impact pressure measured at the location $P1$, see Fig. 4, is compared with the experiment data obtained by Zhou *et al.* [1999] in terms of the following nondimensional time and pressure:

$$T = t\sqrt{\frac{h_0 g}{l_0^2}}, \quad P(T) = \frac{p(T)}{\rho g h_0}.$$

To demonstrate the superiority of the improved iMPM over the original iMPM, this problem is also studied using 4×4 particles per cell (ppc), respectively. The non-dimensional pressure predictions are compared with the experimental data in Fig. 8. When 2×2 ppc are used, the original iMPM results in significant pressure oscillation which does not present in the predictions of the improved iMPM. The oscillation in the original iMPM disappears when 4×4 ppc are used at the expense of a
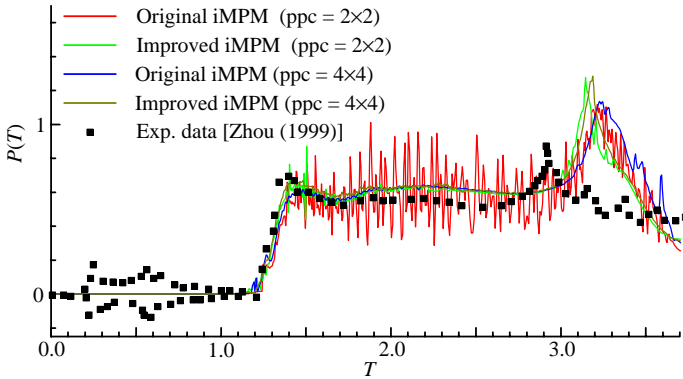
Fig. 8. Comparison of time history of pressure at location $P1$.

significant higher computational cost. This example shows that the improved iMPM with particle shifting not only immensely improves the particle density invariance and the accuracy of velocity field but also suppresses the pressure oscillation.

5.2. *Three-dimensional (3D) dam breaking inside a tank with an obstacle*

To further verify the capability of the proposed method, the collapse of a water column with a rigid obstacle is studied. This problem has also been studied experimentally and numerically by other authors [Kleefsman *et al.* (2005)]. The height of the water column is 550 mm and the size of the rigid obstacle is 403 mm × 161 mm × 161 mm as shown in Fig. 9. The water column is initially closed by a flap. It then flows into the tank when the flap is removed.

The fluid parameters of water and the background grid size are the same as those used in Sec. 5.1. The 3D water column is discretized by 671,000 fluid particles whilst 218,644 ghost particles are located outside the fluid domain and within the static obstacle for correcting the density of the particles near the rigid walls.

Figure 10 shows the fluid profiles and pressure distributions obtained by the improved iMPM at different time instants. During the evolution of the flow, the pressure distribution is smooth and the main flow characteristics agree well with those described by Kleefsman *et al.* [2005] and Amicarelli *et al.* [2013]. In Fig. 10(a), the water front impacts on the obstacle and a water tongue is developed laterally due to the resistance from the rectangular obstacle. In Fig. 10(b), the back wave collides with the downward frontier and then moves on. In Fig. 10(c), a reflecting
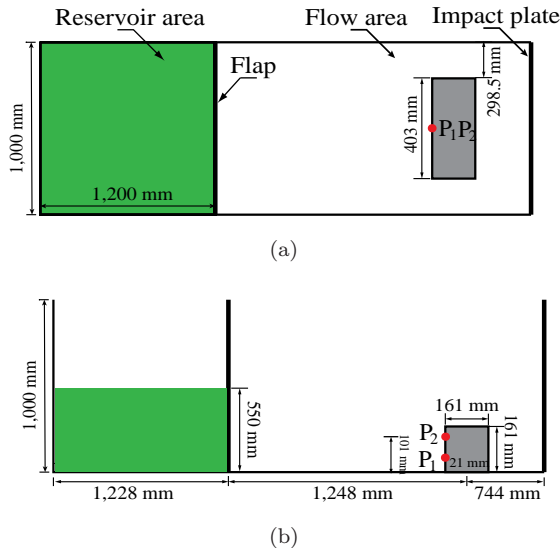
Fig. 9. 3D dam breaking with an obstacle: (a) top view and (b) side view.
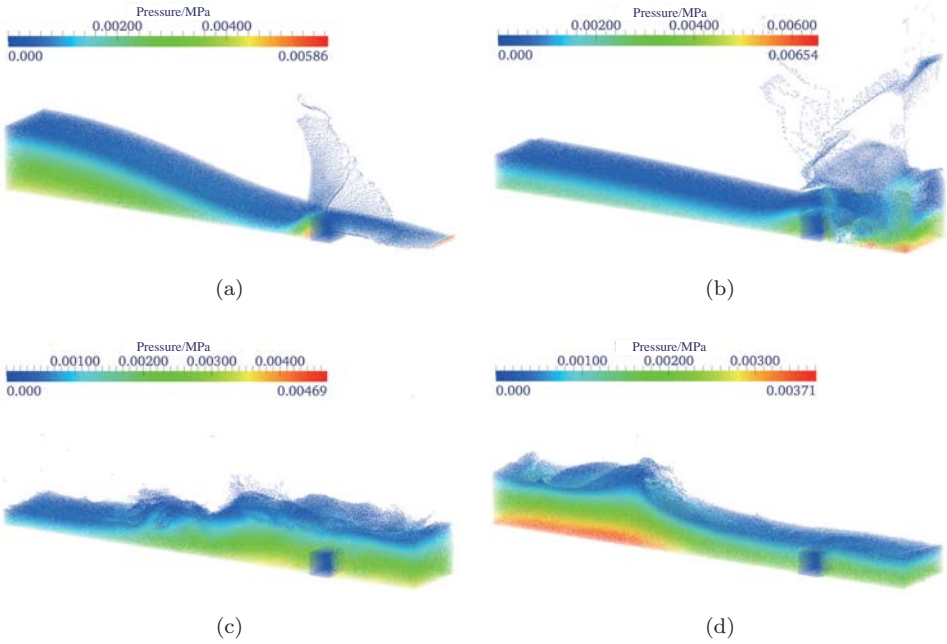
Fig. 10. The pressure distribution of fluid particle at different time instants: (a) $t = 0.6\,\mathrm{s}$, (b) $t = 1.2\,\mathrm{s}$, (c) $t = 2.2\,\mathrm{s}$ and (d) $t = 3.8\,\mathrm{s}$.

steep fronted wave is generated at the right of the tank and the obstacle is completely submerged. In Fig. 10(d), the new water front reaches the original upflow frontier and another reflected front is generated.

To quantitively study the accuracy, the time history of the pressure obtained by the improved iMPM at gauge points P_1 and P_2 are compared with those obtained by δ-SPH method [Marrone $et\ al.$ (2011)] and experiment [Kleefsman $et\ al.$ (2005)] in Fig. 11. The time history of pressure obtained by the improved iMPM agrees reasonably with the experimental results, although some overestimation occurs when plunging wave or spray drops into the water surface again. The pressure at points
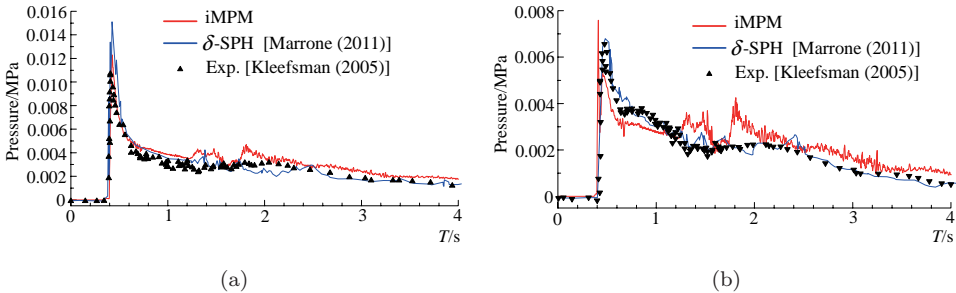
Fig. 11. Time history of pressures at (a) gauge point P_1 and (b) gauge point P_2.

near the free surface fluctuates more intensively than that at other points, which has also been observed in other numerical methods such as the Volume of Fluid [Kleefsman *et al.* (2005)] and weak compressible SPH [Amicarelli *et al.* (2013); Gilbert (2015)]. The main reason is that violent flow occurs close to the free surface. On the contrary, the underwater flow away from free surface is less violent than that the flow close to free surface. These explain why the lower plot contains less ripples than the upper plot. The prediction of the δ-SPH method is exceptionally smooth because an artificial numerical dissipation term was employed to smooth the pressure.

5.3. 2D *water tank sloshing*

In this example, the improved iMPM is used to simulate the water sloshing experiments conducted by Faltinsen *et al.* [2000]. A tank with length $L_B = 1.730$ m stores water with initial depth $H_W = 0.6$ m as shown in Fig. 12. The tank is displaced horizontally and the displacement is $S = A\cos(2\pi t/T)$, where $A = 0.032$ mm is the amplitude and T is period of the excitation. A probe was placed on the initial free surface for recording the water level change H at 0.05 m from the left wall of the tank in the sloshing process.

This experiment is simplified as a 2D problem whilst the two cases with $T = 1.5$ s and $T = 1.3$ s are considered. The water column is discretized by 40,000 fluid particles and 2,327 ghost boundary particles are employed. The computational domain is 1.75 m × 1.17 m which is discretized into uniform cells with side length 0.01 m. In the iMPM simulation, the external excitation is realized as a body force b in Eq. (3), i.e., $b = A(2\pi/T)^2 \cos(2\pi t/T)$. As the water column begins to move rightward, water particles will run up along the right wall. After reaching the maximum height, they gradually fall down and continue to move back and forth. The amplitude of the fluid motion would vary with the natural period T of the sloshing. In Fig. 13, the fluid profiles and pressure distributions are shown at different time instants for $T = 1.5$ s.
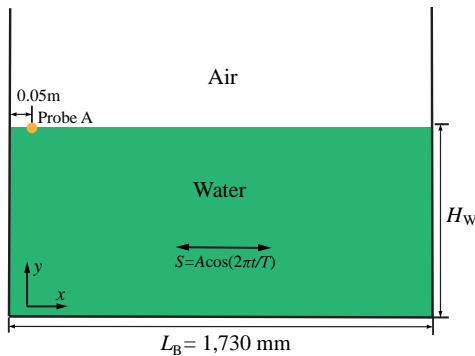
Fig. 12. Illustration of 2D water sloshing in rectangular tank.
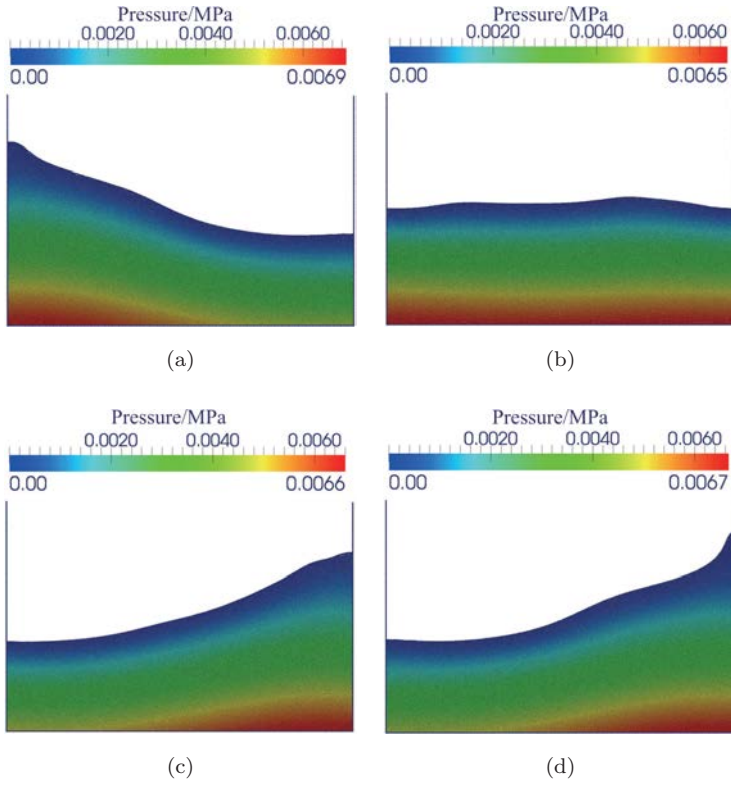
Fig. 13. The fluid profiles and pressure distributions at (a) $t = 7.75\,\mathrm{s}$, (b) $t = 8.00\,\mathrm{s}$, (c) $t = 8.25\,\mathrm{s}$ and (d) $t = 8.50\,\mathrm{s}$.
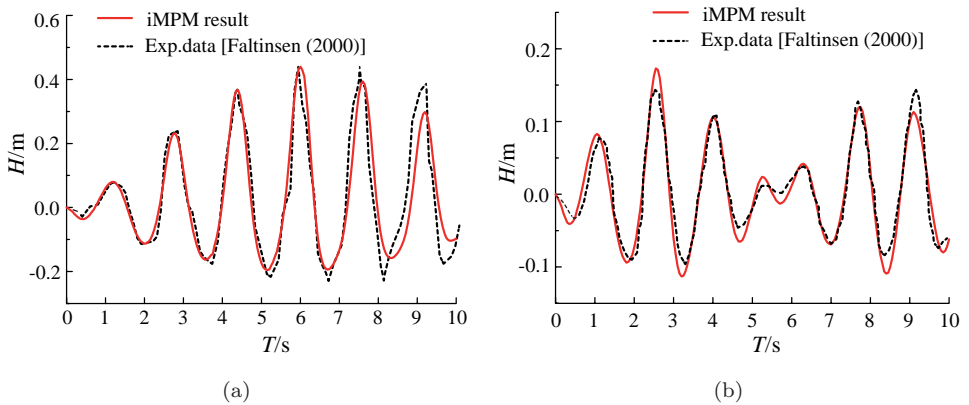
Fig. 14. Time history of the wave height for cases (a) $T = 1.5\,\mathrm{s}$ and (b) $T = 1.3\,\mathrm{s}$.

Figure 14 compares the time history of the water heights obtained by our simulation and recorded by the probe in the experiments [Faltinsen *et al.* (2000)]. For this moderate intensive flow, the flow pattern, period and amplitude predicted by the improved iMPM agree well with the experimental results.

6. Conclusions

In this paper, a density correction scheme is proposed to improve the iMPM. By explicitly imposing the density-invariant condition, a new particle shift scheme is developed based on the kernel approximation. The improved iMPM has following advantages: (1) our density correction scheme is derived from the density-invariant condition whilst the existing schemes are based on some kinds of weak spring force or numerical experiences; (2) the proposed density correction scheme does not impose the Poisson equation and can be implemented conveniently; (3) the density correction scheme is applied at each particle to ensure fluid volume conservation which would be destroyed in the WCMPM and the original iMPM; (4) our density correction scheme is inspired by the SPH kernel approximation, so it can be extended directly to ISPH and MPS methods to impose the density-invariant condition.

The numerical results presented in Sec. 5 show that the improved iMPM not only immensely improves the particle density invariance and the accuracy of the velocity field, but also suppresses the spurious pressure oscillation commonly occurring in violent fluid impact problems. In summary, the improved iMPM is a powerful tool for simulating the incompressible fluid flow with free surface.

Acknowledgment

References

Akinci, N., Ihmsen, M., Akinci, G., Solenthaler, B. and Teschner, M. [2012] "Versatile rigid-fluid coupling for incompressible SPH," *ACM Trans. Graph* **31**(4), 62.

Amicarelli, A., Agate, G. and Guandalini, R. [2013] "A 3D fully Lagrangian smoothed particle hydrodynamics model with both volume and surface discrete element," *Int. J. Numer. Meth. Eng.* **95**(5), 419–450.

Ando, R., Thurey, N. and Tsuruno, R. [2012] "Preserving fluid sheets with adaptively sampled anisotropic particles," *IEEE. Trans. Vis. Comput. Graph* **18**(8), 1202–1214.

Ando, R. and Tsuruno, R. [2011] "A particle-based method for preserving fluid sheets," *Proc. 2011 ACM SIGGRAPH/Eurographics Symp. Computer Animation*, ACM, pp. 7–16.

Asai, M., Aly, A. M., Sonoda, Y. and Sakai, Y. [2012] "A stabilized incompressible SPH method by relaxing the density invariance condition," *J. Appl. Math.* **2012**(11), 2607–2645.

Bardenhagen, S. G., Guilkey, J. E., Roessig, K. M., Brackbill, J. U., Witzel, W. M. and Foster, J. C. [2001] "An improved contact algorithm for the material point method

and application to stress propagation in granular material," *Comput. Model. Eng. Sci.* **2**4, 509–522.

Brackbill, J. U. and Ruppel, H. M. [1986] "FLIP: A method for adaptively zoned, particle-in-cell calculations of fluid flows in two dimensions," *J. Comput. Phys.* **65**(2), 314–343.

Burghardt, J., Leavy, B., Guilkey, J., Xue, Z. and Brannon, R. [2010] "Application of Uintah-MPM to shaped charge jet penetration of aluminum," *IOP Conf. Ser.*, *Mater. Sci. Eng.* **10**(1), 012223.

Chen, Z., Hu, W., Shen, L., Xin, X. and Brannon, R. [2002] "An evaluation of the MPM for simulating dynamic failure with damage diffusion," *Eng. Fract. Mech.* **69**(17), 1873–1890.

Chen, Z., Zong, Z., Liu, M. B. and Li, H. T. [2013] "A comparative study of truly incompressible and weakly compressible SPH methods for free surface incompressible flows," *Int. J. Numer. Meth. Fluids* **73**(9), 813–829.

Chen, Z. P., Qiu, X. M., Zhang, X. and Lian, Y. P. [2015] "Improved coupling of finite element method with material point method based on a particle-to-surface contact algorithm," *Comput. Meth. Appl. Mech. Eng.* **293**, 1–19.

Chorin, A. J. [1968] "Numerical solution of the Navier–Stokes equations," *Math. Comp.* **22**(104), 745–762.

Colin, F., Egli, R. and Lin, F. Y. [2006] "Computing a null divergence velocity field using smoothed particle hydrodynamics," *J. Comput. Phys.* **217**(2), 680–692.

Cummins, S. J. and Rudman, M. [1999] "An SPH projection method," *J. Comput. Phys.* **152**(2), 584–607.

Faltinsen, O. M., Rognebakke, O. F., Lukovsky, I. A. and Timokha, A. N. [2000] "Multidimensional modal analysis of nonlinear sloshing in a rectangular tank with finite water depth," *J. Fluid Mech.* **407**, 201–234.

Foster, N. and Fedkiw, R. [2001] "Practical animation of liquids," *Proc. 28th Annual Conf. Computer Graphics and Interactive Techniques*, ACM, pp. 23–30.

Gilabert, F. A., Cantavella, V. and Mallol, G. [2011] "Modelling fracture process in ceramic materials using the material point method," *Europhys. Lett.* **96**(2), 24002.

Gilbert, J. N. [2015] *Accelerating a Coupled SPH-FEM Solver Through Heterogeneous Computing for Use in Fluid-Structure Interaction Problems*, Ph.D. Thesis, Virginia Polytechnic Institute and State University, Blacksburg, Virginia.

Gui, Q., Shao, S. and Dong, P. [2013] "Wave impact simulations by an improved ISPH model," *J. Waterw. Port Coast. Ocean Eng.* **140**(3), 04014005.

Gui, Q., Dong, P. and Shao, S. [2015] "Numerical study of PPE source term errors in the incompressible SPH models," *Int. J. Numer. Meth. Fluids* **77**(6), 358–379.

Guo, Y. and Nairn, J. A. [2004] "Calculation of *J*-integral and stress intensity factors using the material point method," *Comput. Model. Eng. Sci.* **6**, 295–308.

Harlow, F. H. [1964] "The particle-in-cell computing method for fluid dynamics," *Methods Comput. Phys.* **3**(3), 319–343.

Hu, W. and Chen, Z. [2006] "Model-based simulation of the synergistic effects of blast and fragmentation on a concrete wall using the MPM," *Int. J. Impact Eng.* **32**(12), 2066–2096.

Huang, P., Zhang, X., Ma, S. and Wang, H. K. [2008] "Shared memory OpenMP parallelization of explicit MPM and its application to hypervelocity impact," *Comput. Model. Eng. Sci.* **38**(2), 119–148.

Huang, P., Zhang, X., Ma, S. and Huang, X. [2011] "Contact algorithms for the material point method in impact and penetration simulation," *Int. J. Numer. Meth. Eng.* **85**(4), 498–517.

Ihmsen, M., Cornelis, J., Solenthaler, B., Horvath, C. and Teschner, M. [2014] "Implicit incompressible SPH," *IEEE. Trans. Vis. Comput. Graph* **20**(3), 426–435.

Khayyer, A. and Gotoh, H. [2011] "Enhancement of stability and accuracy of the moving particle semi-implicit method," *J. Comput. Phys.* **230**(8), 3093–3118.

Kleefsman, K. M. T., Fekken, G., Veldman, A. E. P., Iwanowski, B. and Buchner, B. [2005] "A volume-of-fluid based simulation method for wave impact problems," *J. Comput. Phys.* **206**(1), 363–393.

Koshizuka, S., Nobe, A. and Oka, Y. [1998] "Numerical analysis of breaking waves using the moving particle semi-implicit method," *Int. J. Numer. Meth. Fluids* **26**(7), 751–769.

Koshizuka, S. and Oka, Y. [1996] "Moving-particle semi-implicit method for fragmentation of incompressible fluid," *Nucl. Sci. Eng.* **123**(3), 421–434.

Lee, E. S., Moulinec, C., Xu, R., Violeau, D., Laurence, D. and Stansby, P. [2008] "Comparisons of weakly compressible and truly incompressible algorithms for the SPH mesh free particle method," *J. Comput. Phys.* **227**(18), 8417–8436.

Li, J. G., Hamamoto, Y., Liu, Y. and Zhang, X. [2014] "Sloshing impact simulation with material point method and its experimental validations," *Comput. Fluids* **103**, 86–99.

Lian, Y. P., Zhang, X. and Liu, Y. [2011] "Coupling of finite element method with material point method by local multi-mesh contact method," *Comput. Meth. Appl. Mech. Eng.* **200**(47), 3482–3494.

Lian, Y. P., Zhang, X., Zhou, X. and Ma, Z. T. [2011] "A FEMP method and its application in modeling dynamic response of reinforced concrete subjected to impact loading," *Comput. Meth. Appl. Mech. Eng.* **200**(17), 1659–1670.

Lian, Y. P., Zhang, X., Zhang, F. and Cui, X. X. [2014] "Tied interface grid material point method for problems with localized extreme deformation," *Int. J. Impact Eng.* **70**, 50–61.

Liu, M. B. and Li, S. M. [2016] "On the modeling of viscous incompressible flows with smoothed particle hydro-dynamics," *J. Hydrodyn. Ser. B* **28**(5), 731–745.

Liu, M. B., Xie, W. P. and Liu, G. R. [2005] "Modeling incompressible flows using a finite particle method," *Appl. Math. Model.* **29**(12), 1252–1270.

Liu, P., Liu, Y. and Zhang, X. [2015] "Internal-structure-model based simulation research of shielding properties of honeycomb sandwich panel subjected to high-velocity impact," *Int. J. Impact Eng.* **77**, 120–133.

Liu, P., Liu, Y. and Zhang, X. [2016] "Simulation of hyper-velocity impact on double honeycomb sandwich panel and its staggered improvement with internal-structure model," *Int. J. Mech. Mater. Des.* **12**(2), 241–254.

Lobovsk, L., Botia-Vera, E., Castellana, F., Mas-Soler, J. and Souto-Iglesias, A. [2014] "Experimental investigation of dynamic pressure loads during dam break," *J. Fluids Struct.* **48**, 407–434.

Ma, S., Zhang, X. and Qiu, X. M. [2009a] "Comparison study of MPM and SPH in modeling hypervelocity impact problems," *Int. J. Impact Eng.* **36**(2), 272–282.

Ma, S., Zhang, X., Lian, Y. and Zhou, X. [2009b] "Simulation of high explosive explosion using adaptive material point method," *Comput. Model. Eng. Sci.* **39**(2), 101–123.

Marrone, S., Antuono, M., Colagrossi, A., Colicchio, G., Le Touz, D. and Graziani, G. [2011] "SPH model for simulating violent impact flows," *Comput. Meth. Appl. Mech. Eng.* **200**(13), 1526–1542.

Mast, C. M., Mackenzie-Helnwein, P., Arduino, P., Miller, G. R. and Shin, W. [2012] "Mitigating kinematic locking in the material point method," *J. Comput. Phys.* **231**(16), 5351–5373.

Monaghan, J. J. [1985] "Particle methods for hydrodynamics," *Comput. Phys. Rep.* **3**(2), 71–124.

Monaghan, J. J. [1994] "Simulating free surface flows with SPH," *J. Comput. Phys.* **110**(2), 399–406.

Morris, J. P., Fox, P. J. and Zhu, Y. [1997] "Modeling low Reynolds number incompressible flows using SPH," *J. Comput. Phys.* **136**(1), 214–226.

Nair, P. and Gaurav, T. [2015] "Volume conservation issues in incompressible smoothed particle hydrodynamics," *J. Comput. Phys.* **297**, 689–699.

Nairn, J. A. [2007] "Numerical implementation of imperfect interfaces," *Comput. Mater. Sci.* **40**(4), 525–536.

Nestor, R., Basa, M. and Quinlan, N. [2008] "Moving boundary problems in the finite volume particle method," *3rd ERCOFTAC SPHERIC Workshop on SPH Applications*, pp. 2249–2260, 4–6 June 2008, Lausanne, Switzerland.

Onate, E., Idelsohn, S., Zienkiewicz, O. C. and Taylor, R. L. [1996] "A finite point method in computational mechanics. Applications to convective transport and fluid flow," *Int. J. Numer. Meth. Eng.* **39**(22), 3839–3866.

Pan, X. J., Zhang, H. X. and Lu, Y. T. [2008] "Numerical simulation of viscous liquid sloshing by moving-particle semi-implicit method," *J. Mar. Sci. Appl.* **7**(3), 184–189.

Shao, S. and Lo, E. Y. [2003] "Incompressible SPH method for simulating Newtonian and non-Newtonian flows with a free surface," *Adv. Water Res.* **26**(7), 787–800.

Shu, C. W. and Osher, S. [1988] "Efficient implementation of essentially non-oscillatory shock-capturing schemes," *J. Comput. Phys.* **77**(2), 439–471.

Solenthaler, B. and Pajarola, R. [2009] "Predictive–corrective incompressible SPH," *ACM Trans. Graph* **28**(3), 40.

Sulsky, D., Chen, Z. and Schreyer, H. L. [1994] "A particle method for history-dependent materials," *Comput. Meth. Appl. Mech. Eng.* **118**(1), 179–196.

Tan, H. and Nairn, J. A. [2002] "Hierarchical, adaptive, material point method for dynamic energy release rate calculations," *Comput. Meth. Appl. Mech. Eng.* **191**(19), 2123–2137.

Tanaka, M. and Masunaga, T. [2010] "Stabilization and smoothing of pressure in MPS method by quasi-compressibility," *J. Comput. Phys.* **229**(11), 4279–4290.

Tran, L. T., Kim, J. and Berzins, M. [2010] "Solving time-dependent PDEs using the material point method, a case study from gas dynamics," *Int. J. Numer. Meth. Fluids* **62**(7), 709.

Um, K., Baek, S. and Han, J. [2014] "Advanced hybrid particle grid method with subgrid particle correction," *Comput. Graph. Forum* **33**(7), 209–218.

Xu, R., Stansby, P. and Laurence, D. [2009] "Accuracy and stability in incompressible SPH (ISPH) based on the projection method and a new approach," *J. Comput. Phys.* **228**(18), 6703–6725.

Yang, X., Liu, M. and Peng, S. [2014] "Smoothed particle hydrodynamics modeling of viscous liquid drop without tensile instability," *Comput. Fluids* **92**, 199–208.

Yang, X. and Liu, M. [2012] "Improvement on stress instability in smoothed particle hydrodynamics," *Acta Phys. Sin.* **61**(22), 224701.

Yang, X., Peng, S., Liu, M. and Shao, J. [2012]. "Numerical simulation of ballast water by SPH method," *Int. J. Comput. Methods*, **9**(01), 1240002.

York, A. R., Sulsky, D. and Schreyer, H. L. [2000] "Fluidmembrane interaction based on the material point method," *Int. J. Numer. Meth. Eng.* **48**(6), 901–924.

Zhang, X., Chen, Z. and Liu, Y. [2016] *A Continuum-Based Particle Method for Extreme Loading Cases* (Elsevier and Tsinghua University Press).

Zhang, F., Zhang, X., Sze, K. Y., Lian, Y. P. and Liu, Y. [2017] "Incompressible material point method for free surface flow," *J. Comput. Phys.* **330**, 92–110.

Zhou, S., Zhang, X., and Ma, H. [2013]. "Numerical simulation of human head impact using the material point method," *Int. J. Comput. Methods* **10**(04), 1350014.

Zhou, Z. Q., De Kat, J. O. and Buchner, B. [1999] "A nonlinear 3D approach to simulate green water dynamics on deck," *Proc. 7th Int. Conf. Numerical Ship Hydrodynamics*, p. 5.

Zhu, Y. and Bridson, R. [2005] "Animating sand as a fluid," *ACM Trans. Graph.* **24**(3), 965–972.